

Lithospheric thickness, thinning, subduction, and interaction with the asthenosphere beneath China from the joint inversion of seismic S-wave train fits and Rayleigh-wave dispersion curves

Mei Feng ^{a,*}, Suzan van der Lee ^b, Meijian An ^a, Yue Zhao ^a

^a Institute of Geomechanics, Chinese Academy of Geological Sciences, Beijing 100081, China

^b Department of Earth and Planetary Sciences, Northwestern University, Evanston, IL 60208-2150, USA

ARTICLE INFO

Article history:

Received 29 April 2009

Accepted 30 November 2009

Available online 6 December 2009

Keywords:

Upper-mantle structure

Lithosphere thinning

Subduction

Surface-wave inversion

China

ABSTRACT

A joint inversion method of simultaneously inverting regional multimode surface waveforms and fundamental-mode surface wave dispersion curves is used to better constrain a 3-D S-wave velocity model for the upper mantle beneath China. Thousands of broadband vertical-component seismograms were processed, and ~16,500 Rayleigh-wave group-velocity measurements were retrieved at a period of 20 s, with fewer measurements at shorter and longer periods. In addition, 4947 regional Rayleigh waveforms were obtained for paths passing mainly through the Chinese mainland. The joint inversion of this dataset provides new S-wave velocity structures at upper-mantle depths down to 400 km. In particular, the new model is resolved to greater depths than the approximately 200 km depth obtainable in most fundamental-mode surface-wave tomographic studies, and is better resolved at shallow lithospheric depths than that possible in teleseismic body-wave tomographic studies. Because the upper-mantle S-wave velocity is controlled mainly by temperature rather than by composition, thermal structures estimated from the tomographic S-wave velocity model are used to estimate the thickness of the lithosphere beneath China. The results indicate that in eastern China, the North China craton and the Yangtze craton are characterized by pronounced variations in lithospheric thickness, with the lithosphere thinning from west to east. The underlying low-velocity layer and deeper-level high velocities provide important evidence in support of the idea that lithospheric thinning beneath eastern China is related to the westward subduction of oceanic lithosphere to the east and related thermal and dehydration processes. Beneath western China, thickened lithosphere is imaged beneath the Qinghai-Tibetan Plateau, except for beneath Qiangtang in the northern part of the plateau, which is underlain by low velocities. The present model generally supports the interpretation of low velocities beneath Qiangtang as mantle material squeezed out by convergence between the Indian and Asian lithospheres. Moreover, two separate segments of the subducting Indian lithosphere are imaged, indicating that the deeper portion of the subducting slab may have started to break off from the shallower portion as early as 20 Ma.

© 2009 Elsevier B.V. All rights reserved.

1. Introduction

The Chinese mainland, which forms the core of East Asia (Fig. 1), is a continent comprising several large orogenic belts and Precambrian cratons, such as the Qingling-Dabie orogenic belt in central China, the Sino-Korean craton (also termed the North China craton) in north China, the Yangtze craton in central China, and the Tarim craton in northwest China. In addition to the collision zone between the Qinghai-Tibetan Plateau and the Indian subcontinent in southwest China and the eastern marginal sea basins, the geology of many regions in mainland China has been overprinted by major tectonic

events during the Phanerozoic. The youngest tectonic events in East Asia are the northeastward collision of the Indian subcontinent with the Eurasian continent (which started at ~50 Ma) and westward subduction of the Pacific and Philippine Sea plates beneath eastern China (which started at the end of the Mesozoic).

The present tectonic framework of China is controlled by the complex interactions among the Indian subcontinent, the Pacific Plate, the Philippine Sea Plate and the Eurasian continent (Ren et al., 1999). Previous geological studies have provided evidence that Cenozoic crustal deformation of the Chinese mainland has resulted from Indo-Asian collision and from the subduction of oceanic lithosphere (e.g., Darby et al., 2005). Geophysical studies have imaged over-thickened crust and lithosphere beneath the Qinghai-Tibetan Plateau and intensely deformed cratonic lithosphere beneath eastern China (e.g., Huang et al., 2003; An and Shi, 2006; Chen et al., 2008), providing

* Corresponding author. Institute of Geomechanics, MinZu DaXue NanLu 11, Beijing 100081, China. Tel.: +86 10 68482470; fax: +86 10 68422326.

E-mail address: mei_feng_cn@yahoo.com.cn (M. Feng).

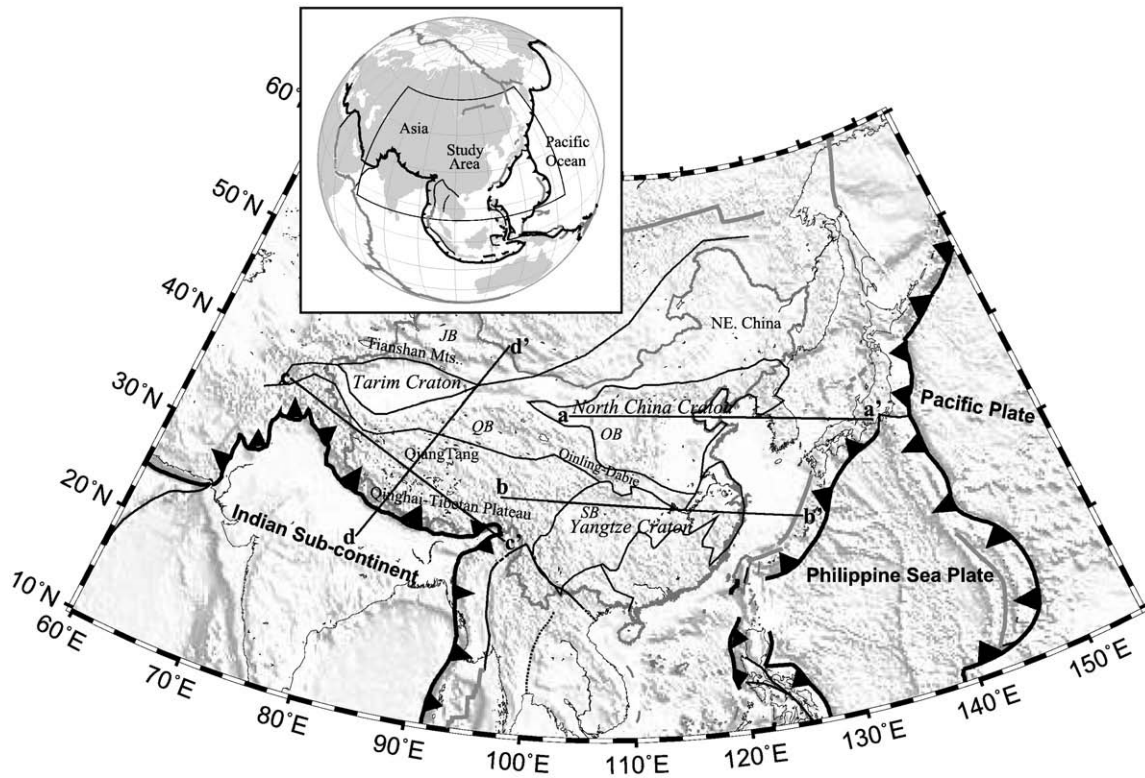


Fig. 1. Simplified tectonic map of East Asia, also showing topography, where JB, QB, OB, and SB denote the Junggar Basin, Qaidam Basin, Ordos Basin, and Sichuan Basin, respectively. Tectonic boundaries are modified from Ren et al. (1999). The transects labeled a–a', b–b', c–c', and d–d' are shown in Fig. 6.

further evidence for interaction among the Indian, Asian, and oceanic plates. However, the mechanism by which such interactions have influenced the lithosphere and asthenosphere beneath the Chinese mainland remains unclear.

A global study of Precambrian lithosphere showed a correlation between crustal age and lithosphere thickness (Artemieva and Mooney, 2001). For example, the North American Archaean Provinces (>2.5 Ga), including the Slave craton, have lithosphere thicknesses of ~250 km (Van der Lee, 2001), while Proterozoic North American lithosphere is 200–180 km thick (Van der Lee, 2002). The Siberian platform (Priestley and Debayle, 2003), the Amazonian craton (Feng et al., 2007), and the Archaean part of the Australian continent have lithosphere thicknesses of ~250–200 km (Simons and Van der Hilst, 2002). However, the age–thickness correlation becomes more complex at a regional scale (Simons and Van der Hilst, 2002) and in tectonically complex regions such as China (An and Shi, 2006). Lithospheric thickness in China appears less related to crustal age and more to tectonic setting (An and Shi, 2006). Therefore, the topography of the lithosphere–asthenosphere boundary beneath the Chinese mainland is poorly predicted based on geographic variations in crustal age. Exploring China's deep upper-mantle structure is therefore essential for understanding lithospheric evolution in this region and the interaction between lithosphere and underlying asthenosphere.

Seismic tomography is a powerful tool for exploring the three-dimensional nature of deep seismic velocity structures beneath China (Ritzwoller et al., 2002; Friederich, 2003; Huang et al., 2003; Feng et al., 2004, 2007; Huang and Zhao, 2006). However, the use of different types of seismic observations can result in seismic velocity structures with different sampling resolution. For example, because the ray paths of body waves are steeply inclined beneath seismic stations, teleseismic body-wave tomography (e.g., Replumaz et al., 2004; Huang and Zhao, 2006; Li et al., 2006a) has good horizontal resolution but poor vertical resolution, especially at shallow lithospheric depths. In contrast, surface-wave dispersion tomography has limited horizontal resolution but good vertical resolution at shallow mantle

depths. Therefore, surface-wave tomography has been preferentially applied in studies of lithospheric structure, whereas body-wave tomography has been applied in studies of deep mantle structures.

Surface-wave tomography using fundamental-mode dispersion measurements (Ritzwoller and Levshin, 1998; Huang et al., 2003) yields reliable resolution for depths shallower than ~200 km, which is not always sufficiently deep to detect the lithosphere–asthenosphere boundary, as the root of cratonic/collision-zone lithosphere may extend deeper than 200 km.

Tomography using multimode surface waveforms (Friederich, 2003; Lebedev and Nolet, 2003; Priestley et al., 2006) can provide reliable resolution down to 400 or more km, as waveforms include higher-mode branches that are sensitive to deep structures. However, this type of modeling requires parameters of focal mechanisms that are only available for strong earthquakes; consequently, for a given database, multimode surface waveform tomography normally yields inferior path coverage to that for fundamental-mode surface-wave dispersion tomography, and thus has lower resolution at shallower depths.

To improve the resolution both within and around the base of the lithosphere, a modified formulation of surface-wave tomography was adopted to enable the use of both fundamental-mode surface-wave dispersion measurements and multimode surface waveforms to constrain an upper-mantle 3-D S-wave velocity (β) model. The jointly constrained model combines the advantages of the good path coverage of fundamental-mode dispersion observations and good sensitivity to deep structures of multimode waveforms, thereby yielding superior horizontal and vertical resolution compared with previous models constrained only by one type of surface-wave observation (Friederich, 2003; Huang et al., 2003; Priestley et al., 2006). Because the upper-mantle S-wave velocity anomalies are controlled mainly by spatial variations in temperature rather than composition, lithospheric thickness beneath China is estimated by converting the inferred upper-mantle S-wave velocities to temperature, following An and Shi (2006, 2007), Goes et al. (2000), McKenzie and Priestley (2008), Priestley and McKenzie (2006), and Shapiro and Ritzwoller (2004),

among others. A discussion on the dynamics is given according to variations of lithospheric thickness among tectonic domains.

2. Seismic data

The upper-mantle *S*-wave velocity model proposed in the present study is jointly constrained by fundamental-mode Rayleigh wave group-velocity dispersion curves and multimode Rayleigh waveforms. The former is used mainly to constrain shallow structures, whereas the latter is also sensitive to deep structures. The analyzed seismograms were recorded by 283 permanent and temporary broadband stations deployed in and around China before 2006 (triangles in Fig. 2). The permanent networks include New China Digital Seismograph Network, the Broadband Array in Taiwan, GEOSCOPE, Global Seismographic Network, and the Kazakhstan Network, among others. The temporary networks/arrays include experiments deployed upon the Tibetan Plateau, in North China, and in NE China, among others, generally with several years of scheduled operation.

Because fundamental-mode dispersion measurements are mainly used to constrain shallow structures in the present study, and because observational uncertainties show a marked increase for long propagation paths and long periods, fundamental-mode group velocities were only measured for periods from 10 to 160 s for wave paths

located entirely within the study region. In total, we obtained ~16,500 measurements for a period of 20 s and fewer measurements for shorter and longer periods. Fig. 2a shows the path density of the fundamental-mode group-velocity measurements for a period of 20 s. The density is defined as the number of paths that cross each 1° by 1° ($\sim 10,000$ km²) area. Most regions of China have a path density in excess of 100 paths, which represents a dramatic advance compared with earlier studies; e.g., Huang et al. (2003) analyzed about 4000 dispersion curves. Because path coverage of seismic data is essential in achieving high tomographic resolution, the inclusion of a large number of fundamental-mode measurements enables us to tightly constrain lithospheric *S*-wave velocity structures beneath the Chinese mainland.

Multimode Rayleigh waveforms (Fig. 2b) are selected mainly from the same seismogram bank from which fundamental-mode group-velocity measurements were obtained. In total, 4947 multimode Rayleigh waveforms were analyzed using a slightly modified form of the Partitioned Waveform Inversion (PWI) package (Van der Lee and Nolet, 1997). Fig. 2b shows the path density of the multimode waveforms: most of the continental region has a path density greater than 50 paths. Waveform data were analyzed using hypocenter locations and event origin times from the Engdahl–Hilst–Buland (EHB) catalogue (Engdahl et al., 1998) updated through 2006, and

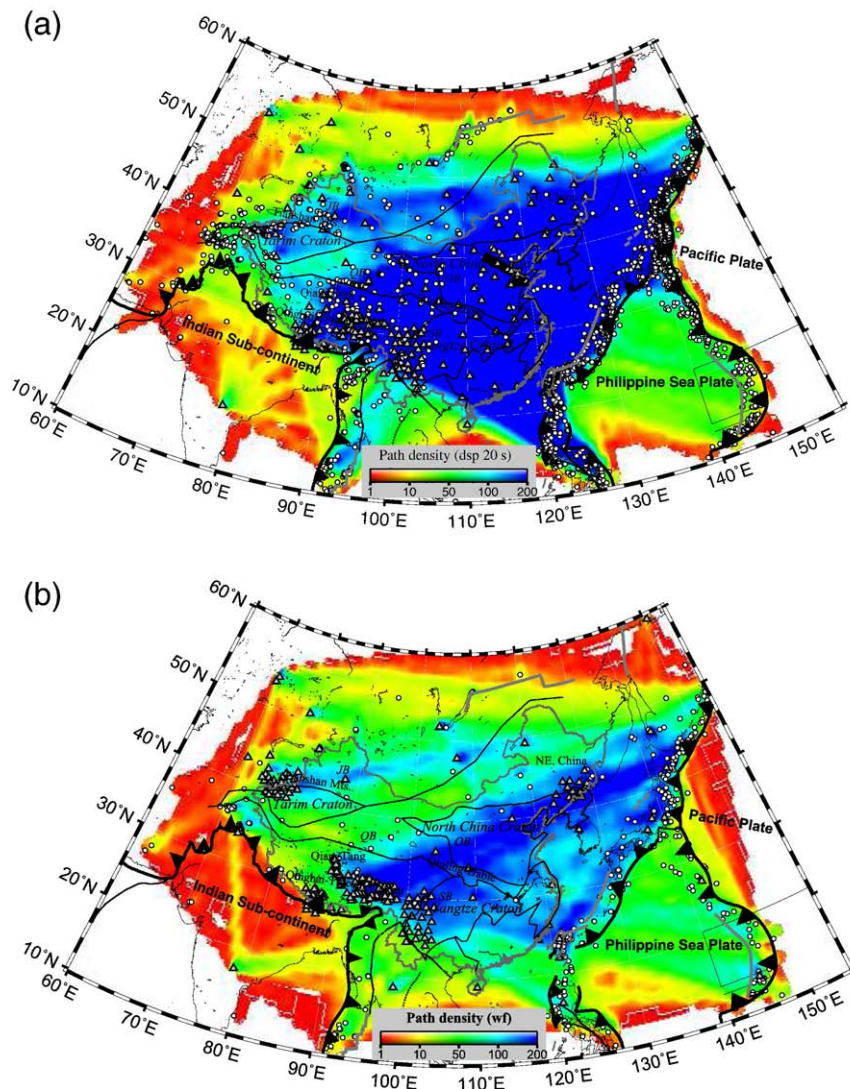


Fig. 2. Path density of fundamental-mode group-velocity measurements at a period of 20 s (a) and of multimode waveforms (b). The density is defined as the number of paths that cross each $1^\circ \times 1^\circ$ area. Triangles and circles represent seismic stations and epicenters used to form the final surface-wave databank, respectively.

moment tensor solutions from the Global Centroid Moment Tensor database (Dziewonski et al., 1983).

In previous multimode tomographic studies (Van der Lee et al., 2001; Feng et al., 2007), fewer than 2000 waveforms were generally considered because each seismogram was subjected to substantive quality control and the waveforms were fitted interactively using the PWI package. In the present study, the processing procedure was modified to enable semi-automatic waveform processing. In this modified procedure, the waveforms were fitted automatically using default parameter settings, and waveforms with good fits were selected during a later interactive checking stage. The 4947 multimode waveforms fitted using the new procedure represents a significantly larger number than the ~1600 waveforms used in an earlier study of upper-mantle *S*-wave velocity structure in East Asia (Friederich, 2003).

Performing measurements of fundamental-mode group velocity only requires knowledge of the hypocenter location and event origin time; consequently, it can be applied to relatively small earthquakes, whereas waveform modeling requires earthquake moment tensor solutions that are generally only available for relatively large earthquakes ($m_b > 5.5$) (Feng et al., 2007). Therefore, for a given seismogram database, many more fundamental-mode group-velocity measurements (i.e., better path coverage) are retrieved than are multimode waveform fits (Fig. 2). The joint inversion of the two datasets performed in the present study is intended to combine the advantages of the better path coverage of fundamental-mode group-velocity measurements and the better depth sensitivity of multimode waveforms.

To moderate the trade-off between Moho depth and uppermost upper-mantle *S*-wave velocities, and thus to improve the resolution of deep lithospheric structures, we invert for Moho depth together with *S*-wave velocities. This model parameterization works well in retrieving mantle structures but is too coarse for useful interpretations of crustal and sub-Moho structures. Therefore, *S*-wave velocity structures in the crust or near the Moho are not interpreted. However, to better separate crustal structure from mantle structure in the present inversion, 5461 point constraints of crustal thickness are used from previous receiver function analyses and studies of seismic reflection/refraction (e.g., Mangino et al., 1999; Galvé et al., 2002; Gao et al., 2005; Li et al., 2006b). These point constraints are included in the present inversion in the manner suggested by Van der Lee and Nolet (1997), which ensures that the crustal thickness model is compatible with independent observations of crustal thickness.

3. Surface wave tomography

Feng et al. (2007) developed a method for the joint inversion of fundamental-mode group-velocity measurements and multimode surface waveforms, and successfully applied this procedure in a study of upper-mantle structure beneath South America. Here, the method developed by Feng et al. (2007) is improved in several aspects. The method is briefly summarized below.

The joint inversion of multimode surface waveforms and fundamental-mode group velocities is based on the basic concept of inversions using independent observations. Multimode surface waveform inversion generally involves two steps (Van der Lee and Nolet, 1997): (1) waveform fitting to determine the 1-D average structure along each path, and (2) linear inversion of all 1-D path-averaged constraints to obtain the 3-D structure. The conventional approach to the inversion of group velocities for 3-D *S*-wave velocities also requires two steps (e.g., Ritzwoller et al., 2002; Feng et al., 2004): (1) period-by-period inversion for group-velocity maps, and (2) cell-by-cell (point-based) inversion of regionalized group velocities for 1-D *S*-wave velocity structures.

In their 3-D joint inversion, Feng et al. (2007) combined the path-averaged structure constraints derived from waveform fitting and point-based constraints derived from the linearized relation between regionalized dispersion curves and 1-D *S*-wave velocity structures. Here, point-based constraints were not used from the linearized

relation between the regionalized dispersion curve and 1-D *S*-wave velocities, but we directly use constraints from the linearized relation (An et al., 2009) between event-to-receiver dispersion measurements and 3-D *S*-wave velocities; this approach represents a modification of the two-step group-velocity inversion described above. To derive the final 3-D structure model, the 1-D path-averaged structure constraints derived from waveform fitting are combined with the linearized constraints derived from dispersion curves.

In the partitioned waveform inversion method, the 3-D model \mathbf{m} is discretized as a Cartesian grid, which differs from the geographical grid normally used in group-velocity tomography. To prevent the inconvenience and potential source for error caused by different parameterizations in the waveform and dispersion constraints (see Feng et al., 2007), we unify the model parameterization to geographical grids at a series of depths, with a constant horizontal spacing measured in degrees.

The linear relation between the 3-D model \mathbf{m} and the combined constraints from waveform fitting and group-velocity inversion can be described as follows:

$$\begin{pmatrix} \mathbf{H}_w \\ \lambda_d \mathbf{H}_d \\ \lambda \mathbf{S} \end{pmatrix} \mathbf{m} = \begin{pmatrix} \mathbf{q}_w \\ \lambda_d \mathbf{q}_d \\ \mathbf{0} \end{pmatrix}$$

where \mathbf{H} and \mathbf{q} represent a sensitivity matrix and data vector, respectively; \mathbf{m} is the 3-D model to be determined; the subscripts *w* and *d* represent constraints derived from waveforms and fundamental-mode group velocities, respectively; and λ_d is a penalty for the group-velocity dispersion constraints. Because the sensitivity matrices \mathbf{H}_w and \mathbf{H}_d are large and sparse, *a priori* constraints are required to stabilize the linear inversion. Here, we introduce the first gradient of the model (\mathbf{S}), instead of the minimum norm used in Feng et al. (2007), as an *a priori* smoothing constraint to produce a more physically reasonable model. Both λ_d and λ are determined by trial and error to search for a reasonable 3-D model that provides a sufficient fit to both waveforms and regionalized group-velocity dispersions.

The program LSQR (Paige and Saunders, 1982a,b) was used to resolve the model \mathbf{m} in the above equation. Uncertainties in the tomographic model \mathbf{m} (*S*-wave velocities) are difficult to quantify because they are caused by many factors, including theoretical approximations, choice of reference model, weighting of damping/smoothing, path density, path azimuthal distribution, frequency content, and mode composition of surface waves. Inversion of both Rayleigh-wave group and phase velocity observations may result in an *S*-wave velocity uncertainty of 0.02–0.1 km/s for depths down to 120 km (Rapine et al., 2003); the difference in *S*-wave velocity uncertainty resulting from linearized surface-wave inversion (Snoko and James, 1997) and from the global searching method (Snoko and Sambridge, 2002) is less than ~0.04 km/s (An and Assumpção, 2006). Inversion using only group velocities would result in greater uncertainty in *S*-wave velocity than that obtained using both group and phase velocities (Shapiro and Ritzwoller, 2002); however, the present joint inversion using both group velocities and multimode waveforms yields lower uncertainty than that obtained for inversion using only group velocities. Therefore, an uncertainty of ~0.1 km/s is assumed in the present *S*-wave velocity model.

A checkerboard test is a useful indicator of the spatially varying resolving power of seismic tomography. Considering the coverage of seismic data in the present study, the study region is defined as 60–155°E in the *x* (longitude) direction and 10–60°N in the *y* (latitude) direction. The final *S*-wave velocities are computed on 3-D grids with a spacing of 1° in the *x* and *y* directions and 20 km in the *z* (depth) direction. We used a reference model similar to *iasp91* (Kennett and Engdahl, 1991), but with a crustal thickness of 40 km, which is the average crustal thickness of the Chinese continent.

Fig. 3 shows the results of the checkerboard test using the same path coverage and depth sensitivity as employed in constructing the

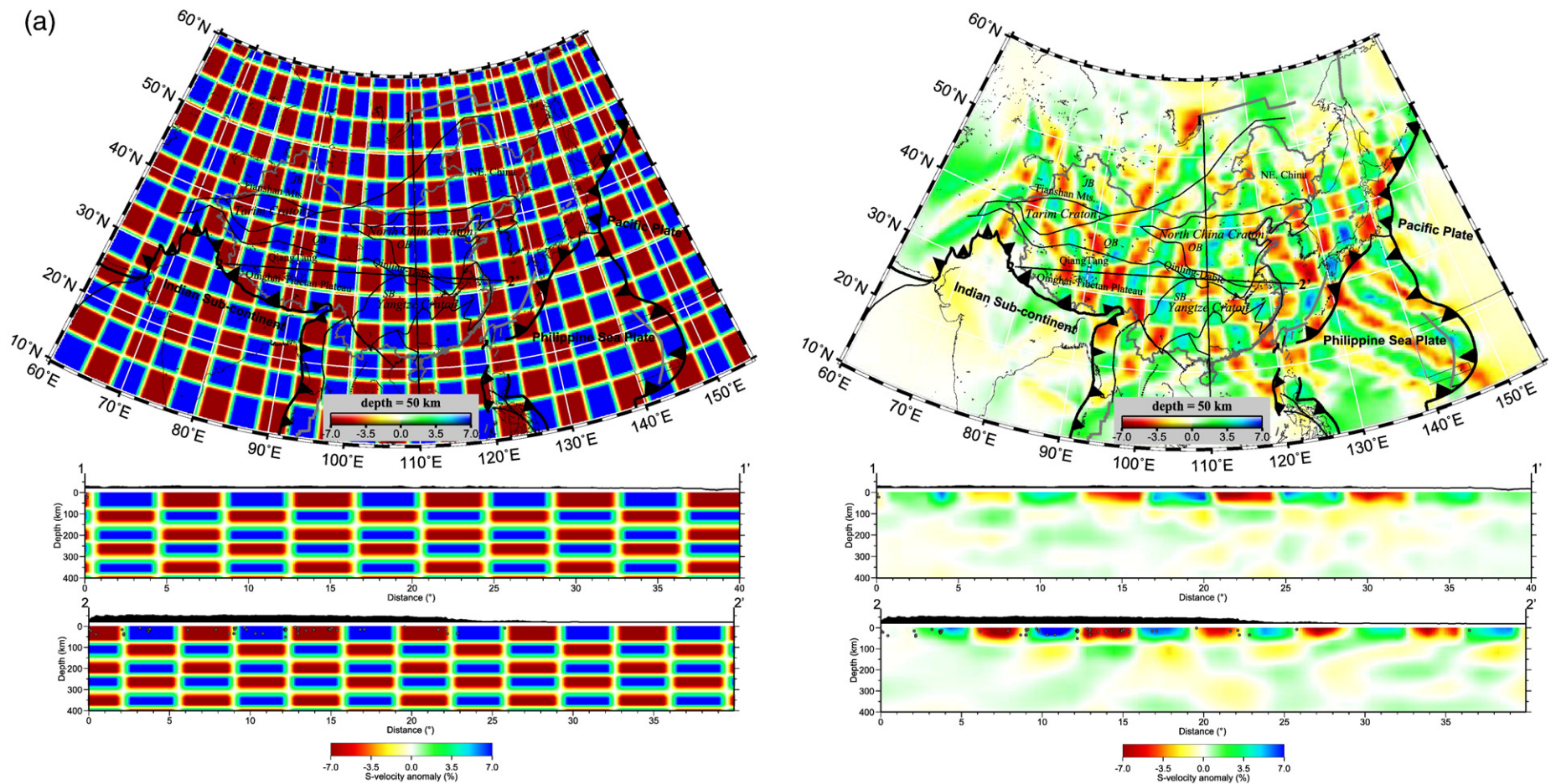


Fig. 3. Horizontal and vertical *S*-wave velocity slices showing the results of checkerboard tests. The sizes of 3-D checkers are as follows: (a) $4^\circ \times 4^\circ \times 80$ km, (b) $6^\circ \times 6^\circ \times 120$ km, and (c) $8^\circ \times 8^\circ \times 160$ km. The left column shows slices of the input model, and the right column shows slices of the retrieved model. The locations of vertical transects are shown in the horizontal slices.

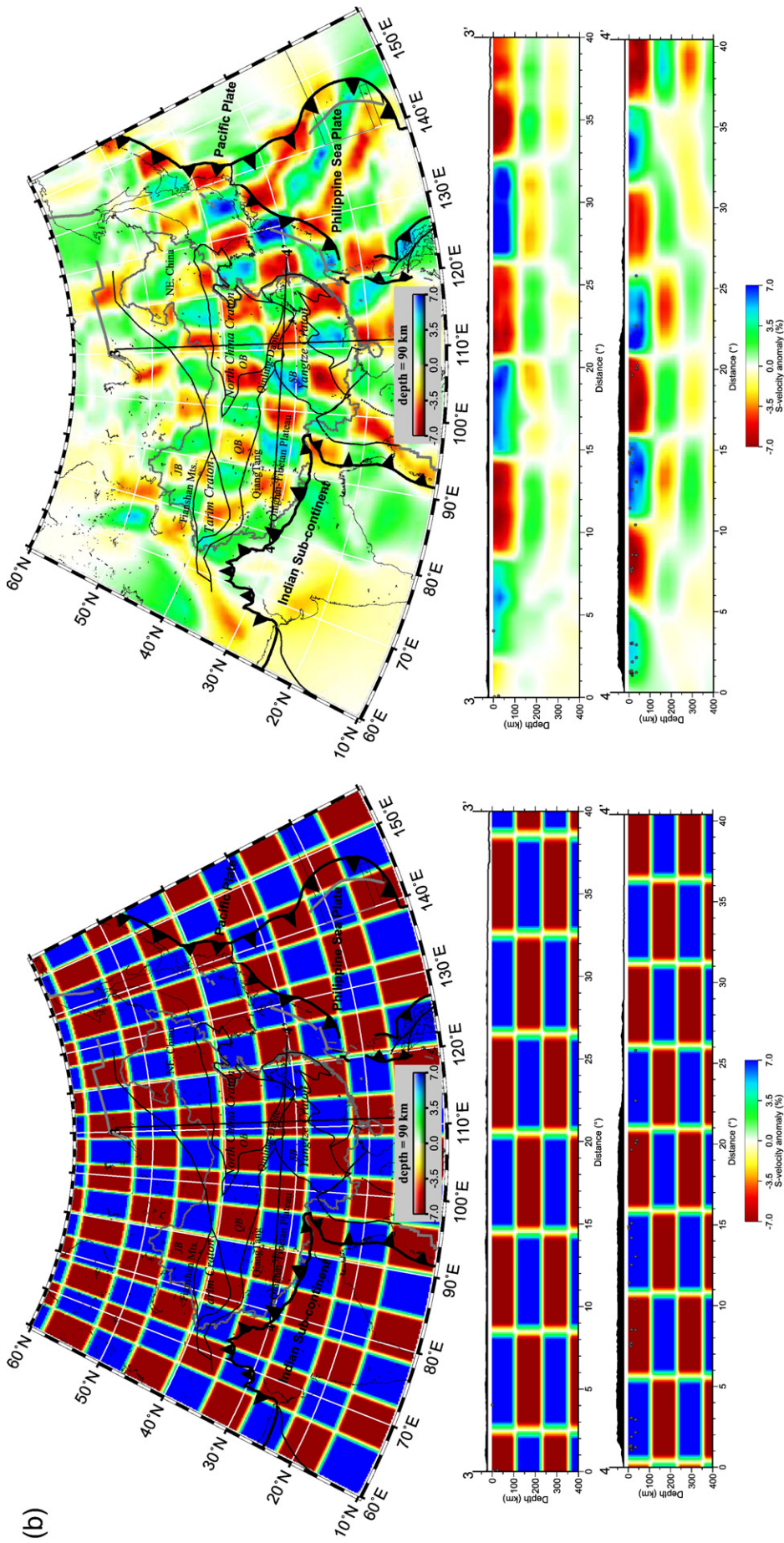


Fig. 3 (continued).

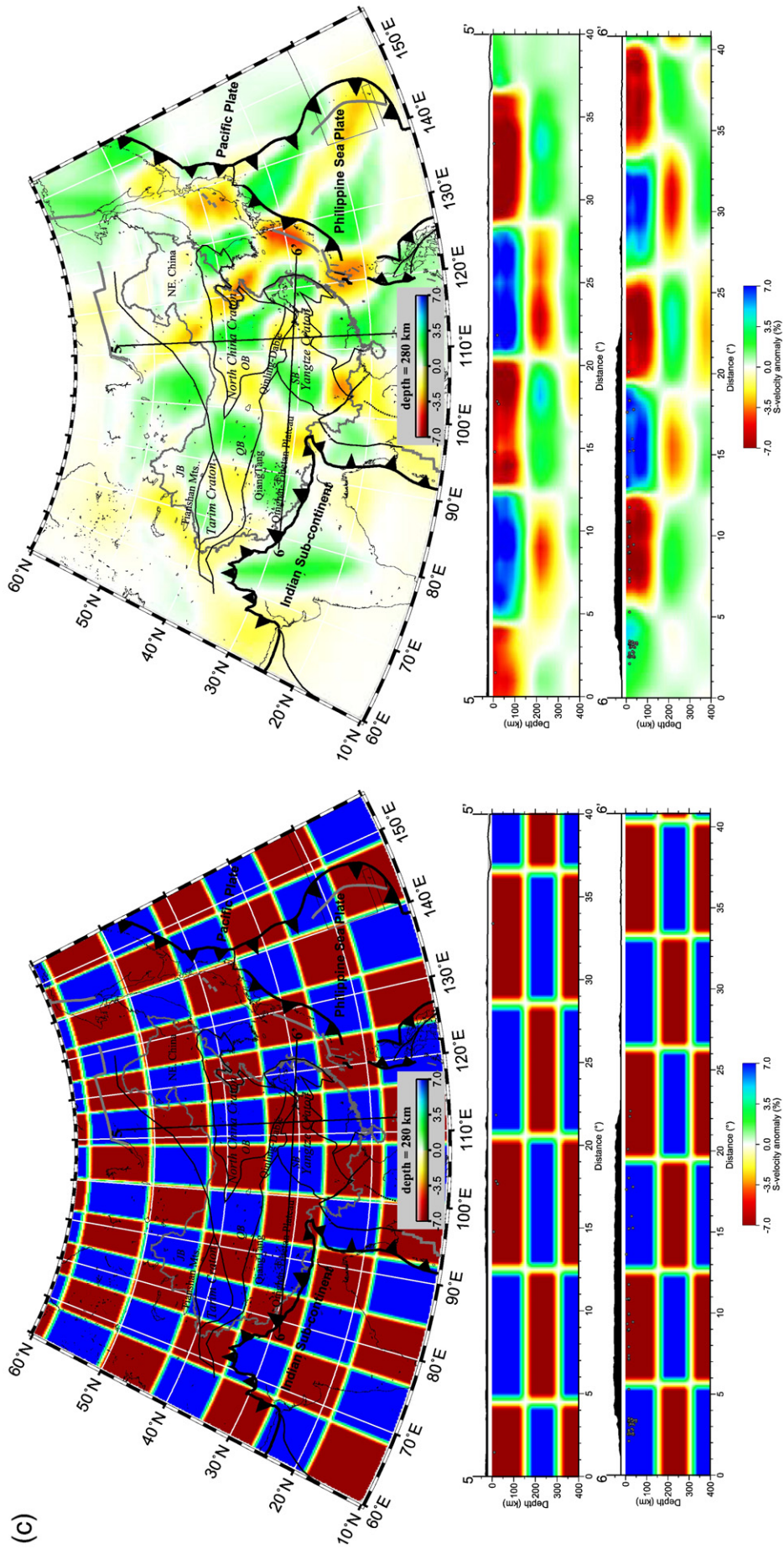


Fig. 3 (continued).

final *S*-wave velocity model. To simultaneously test the horizontal and vertical resolving power, the 3-D synthetic model was set with both horizontally and vertically alternating checkers. The *S*-wave velocity perturbations of the checkers are assigned as $\pm 7\%$ relative to the reference model. Because the sensitivity and resolving power of surface waves show strong variations with depth, synthetic tests were performed with different checker sizes: $4^\circ \times 4^\circ \times 80$ km (~ 400 , ~ 444 , and 80 km in the *x*, *y*, and *z* directions, respectively), $6^\circ \times 6^\circ \times 120$ km, and $8^\circ \times 8^\circ \times 160$ km (Fig. 3). The inverted model of the checkerboard tests retrieved $4^\circ \times 4^\circ \times 80$ km checkers down to ~ 100 km depth (Fig. 3a), $6^\circ \times 6^\circ \times 120$ km checkers down to ~ 200 km depth (Fig. 3b), and $8^\circ \times 8^\circ \times 160$ km checkers down to 400 km depth (Fig. 3c) for most of the Chinese mainland.

Resolution can be defined as half of the recovered checker size (Lebedev and Nolet, 2003). According to this definition, the average horizontal resolution length in the central part of the study region is $\sim 2^\circ$ down to 100 km depth, $\sim 3^\circ$ down to 200 km, and $\sim 4^\circ$ down to 400 km. The average vertical resolution is ~ 40 km down to ~ 100 km depth, ~ 60 km down to 200 km, and ~ 80 km down to ~ 400 km. The resolving power weakens with depth and in marginal regions.

The present results are also compared with previously published tomographic models. Though most previous tomographic models are generally in agreement with regional-scale features, there remain differences in detail due to the use of different numbers and frequency/mode contents of surface waves or different methodologies (Friederich, 2003; Huang et al., 2003; Priestley et al., 2006). The present model shows similar upper-mantle structures to those revealed by the upper-mantle *S*-wave velocity model of East Asia constructed by Friederich (2003), who took advantage of the Fresnel zones of the data by using exact 3-D waveform sensitivity kernels that correctly reflect off-path sensitivity. Although ray-theory approximation is used in the present study, the large number of surface wave data counterbalances the lack of finite-frequency effects in ray theory (Sieminski et al., 2004), thereby yielding structural details in the present model that are comparable to those in an advanced tomographic model constrained by exact 3-D waveforms.

4. Conversion of *S*-wave velocity to temperature

Because of (1) the smoothly depth-dependent sensitivity of the present data and (2) the regularization applied in the present joint inversion, the base of the lithosphere in the present *S*-wave velocity model does not correspond to a sharp change in seismic velocity. Consequently, it is necessary to derive a different indicator from the *S*-wave velocities that represents the lithosphere–asthenosphere boundary. Temperature is the best physical parameter in this regard because it is the dominant factor in determining the strength of mantle materials. In addition, many seismic studies (e.g., Jordan, 1979; Nolet and Zielhuis, 1994; Sobolev et al., 1996; Schuberth et al., 2009) have shown that temperature is the dominant effect on upper-mantle (and even lower mantle) seismic velocities, with composition playing a lesser role.

Based on a given upper-mantle composition, laboratory measurements of density and elastic moduli for various mantle minerals at high temperatures and pressures can be used to estimate the upper-mantle temperature field from a 3-D *S*-wave velocity tomographic model. Such seismic–thermal analysis has been widely used in previous studies (Goes et al., 2000; Goes and Van der Lee, 2002; Cammarano et al., 2003; Shapiro and Ritzwoller, 2004; Priestley and McKenzie, 2006). In addition, Van der Lee (2001) reported a remarkable agreement between (1) the depth of the steepest negative velocity gradient with depth (representing the seismic thickness of the lithosphere) and (2) the depth to the 1200°C isotherm (representing the thermal thickness of the lithosphere) beneath the central and eastern US. For China, An and Shi (2006) demonstrated that the base of the seismic lithosphere (or top of the low-velocity zone) agrees well with the

thermal base of the lithosphere, defined as the depth to a temperature of 1300°C .

The present analysis reveals that the isotherm value representative of the base of the lithosphere could vary in the case that temperatures are estimated from an *S*-wave velocity model constrained by different datasets; consequently, the contrasting isotherms identified as representing the base of the lithosphere beneath the U.S. (Van der Lee, 2001) and China (An and Shi, 2006) might reflect the fact that the former temperature model was derived from *S*-wave velocities constrained by multimode surface waveforms, whereas the later was derived from *S*-wave velocities constrained by measurements of fundamental-mode surface-wave dispersion. In the present study, because the *S*-wave velocity model is constrained by a combination of both multimode surface waveforms and fundamental-mode surface-wave dispersion, the 1250°C isotherm is chosen to represent the base of the lithosphere. An accurate estimation of lithosphere thickness is important in extracting information on tectonics and geodynamics (Menzies and Xu, 1998; Griffin et al., 1999; O'Reilly et al., 2001; Priestley and Debayle, 2003; An and Shi, 2006; McKenzie and Priestley, 2008).

The crustal thickness of the Chinese mainland ranges from ~ 30 to ~ 80 km; therefore, it is possible that *S*-wave velocities at depths less than ~ 80 km are influenced by low velocities from nearby crust (primarily because of the relatively coarse parameterization employed with respect to the scale of crustal structures and spatial variations in such structures), resulting in an overestimation of temperatures at depth in the crust. Because temperatures estimated in this way are more accurate for deep lithosphere than for regions close to the Moho (McKenzie and Priestley, 2008), *S*-wave velocities are only converted to temperatures for upper-mantle depths greater than 80 km. *S*-wave velocities are converted to temperature using the forward formulations described in An and Shi (2006, 2007), which is a slightly modified version of that proposed by Goes et al. (2000). The forward procedure takes into account both anharmonic and anelastic effects. A direct grid search method is used in the nonlinear temperature inversion.

Slightly different temperatures are obtained for different upper-mantle compositions. The continental upper-mantle composition for different tectonic domains can be simply classified into two categories: an off-cratonic composition (68% olivine, 18% orthopyroxene, 11% clinopyroxene, 3% garnet, and an Fe content of 0.1) and an on-cratonic composition (83% olivine, 15% orthopyroxene, 2% garnet, and an Fe content of 0.086) (e.g., Shapiro and Ritzwoller, 2004 and references therein). The difference between on- and off-cratonic composition is caused not only by Fe content but also by pyroxene content (McDonough and Rudnick, 1998; O'Reilly and Griffin, 2006). The effect of mineral composition can generate velocity anomalies of $< 1\%$ in the shallow mantle, which would be difficult to resolve in seismic tomography (Goes et al., 2000). Consequently, spatial variations in composition are not considered in the temperature conversion. Because most areas in and around the Chinese mainland have been strongly affected by Phanerozoic tectonism, most regions record young tectono-thermal ages. Therefore, an off-cratonic composition was chosen for the Chinese continent.

The results of forward tests (An and Shi, 2006) reveal that an on-cratonic composition can increase the temperature estimation by ~ 15 – 120°C compared with an off-cratonic composition. In addition, the use of a different model to that employed in the present study, with stronger temperature–anelasticity dependency, can lower the obtained temperature estimates by ~ 0 – 180°C (Goes et al., 2000), and an uncertainty in *S*-wave velocity of 0.1 km/s can cause temperature variations in the order of ~ 50 – 250°C .

The presence of fluids (e.g., melt or water) results in a marked reduction in seismic velocities (Hirth and Kohlstedt, 1996; Karato and Jung, 1998; Goes et al., 2000; Avseth et al., 2005). However, because no model has been developed to show the distribution of melt and

fluids in the upper mantle beneath the study area, the effects of melt and fluids are not considered in the present conversion of velocity to temperature. If fluid-affected velocities were interpreted in terms of temperature, temperature would be overestimated. Therefore, relatively high mantle temperature estimated in the present study should be considered as the upper bound, and in the case that the converted temperature for the upper mantle is anomalously high; a possible explanation may be the existence of fluids. The combined effects of various factors on temperature uncertainty may be additive or subtractive, making it difficult to quantify the uncertainty in our temperature model, which may vary from tens to several hundreds of degrees centigrade. The results of An and Shi (2006) and Goes et al. (2000) indicate a temperature uncertainty of $\sim 150^\circ\text{C}$ for the present conversion of S -wave velocity to temperature. The uncertainty is likely to be less than 150°C at depths around the lithosphere–asthenosphere boundary, because the lithospheric thickness estimated in the present study is similar to that estimated in previous studies (see below); a variation in temperature of 140 (or 70) $^\circ\text{C}$ can result in a variation in estimated lithospheric thickness of ~ 40 (or 25) km (see the following paragraph).

Fig. 4 shows two 1-D S -wave velocity profiles (thick dashed lines) and the corresponding converted temperatures using off-cratonic (thin dashed lines) and on-cratonic (dotted lines) compositions; an uncertainty of $\pm 150^\circ\text{C}$ is indicated by shading. The depth at which the converted temperature (thin dashed lines) is closest to the 1250°C isotherm (solid lines) is selected as the base of the thermal lithosphere. Although the difference in temperatures estimated using the two continental compositions is less than 70°C , if the estimated geotherms reach the 1250°C isotherm (as a proxy for the base of the lithosphere) in the convective regime, the difference of 70°C can result in a difference in depth of 25 km or significantly more.

The 1-D S -wave velocity and temperature profiles shown in Fig. 4a and b are taken from North China and central Tibet, respectively. The anomalously high temperature at shallow upper-mantle depths beneath central Tibet (~ 80 – 110 km in Fig. 4b) originates in part

from vertical smoothness constraints and the trade-off between Moho depth (~ 80 km in central Tibet) and S -wave velocities, although this effect becomes much weaker at greater depths and in other regions with thinner crust, as seen in the profile for North China (Fig. 4a). In addition, the high temperature may suggest that variations in seismic velocity beneath the complex structure of Tibet are caused not only by temperature variations but also by varying degrees of dehydration, Fe depletion, and partial melting.

5. Seismic–thermal structures

Here, the S -wave velocities derived from surface-wave tomography are expressed as perturbations ($\delta\beta$) in percentage relative to the reference *iasp91* model (Kennett and Engdahl, 1991), and are shown as horizontal sections at four depths (Fig. 5) and four vertical transects of S -wave velocities (left column) and velocity-derived temperatures (right column) across different tectonic provinces of the Chinese mainland (Fig. 6). The depth at which the estimated temperature is closest to the 1250°C isotherm is interpreted as the base of the lithosphere (dotted lines on the temperature transects). Because vertical transects provide a better sense of both lateral and vertical variations in structure than do horizontal sections at different depths, the following description and discussion focuses on the vertical transects.

Transects a–a' and b–b' in eastern China (Fig. 6) mainly cross the North China craton in the north and the Yangtze craton in the south, respectively, with their easternmost parts approaching the trench where the Pacific Plate and the Philippine Sea Plate, respectively, are subducting beneath Asia. On the eastern part of transect a–a', the westward-subducting Pacific slab, which is accompanied by deep earthquakes, is well imaged as an area of anomalously high S -wave velocity (low temperature) between 300 and 400 km depth. An extensive area of low-velocity mantle wedge is clearly imaged above the slab, near the Philippine Sea slab. A similar mantle wedge is apparent on the eastern part of transect b–b'. The western part of transect a–a'

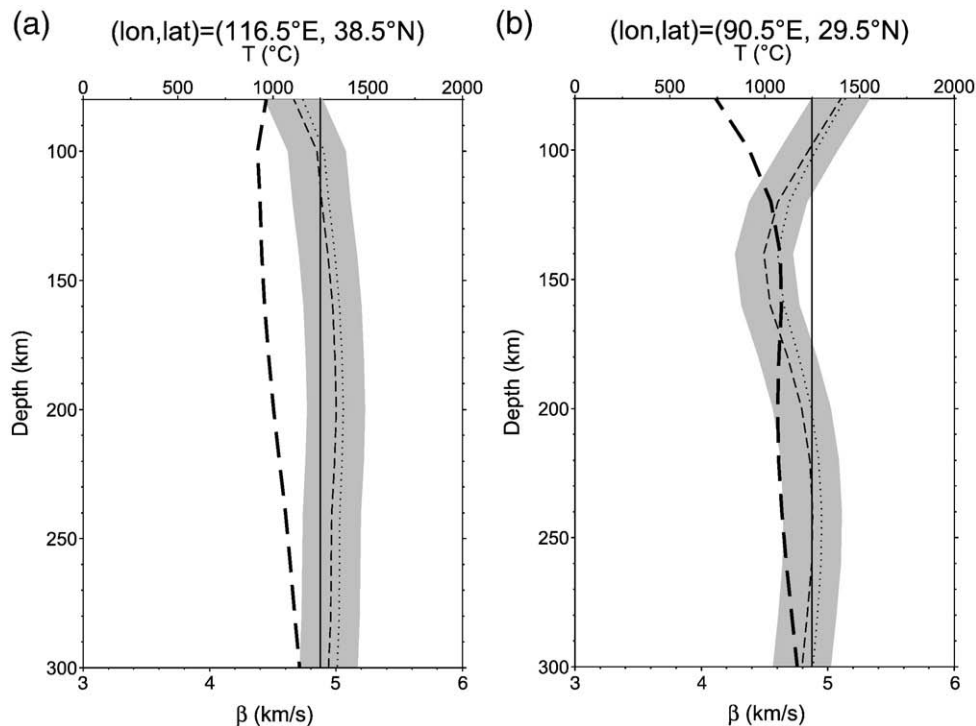


Fig. 4. One-dimensional seismic–thermal profiles taken from North China (a) and central Tibet (b). Thick dashed lines are S -wave velocity obtained from the joint tomographic inversion; thin dashed and thin dotted lines are the converted temperature using off-cratonic and on-cratonic compositions, respectively; the gray shading indicates uncertainties of $\pm 150^\circ\text{C}$ in the estimated temperatures; solid lines are the 1250°C isotherm.

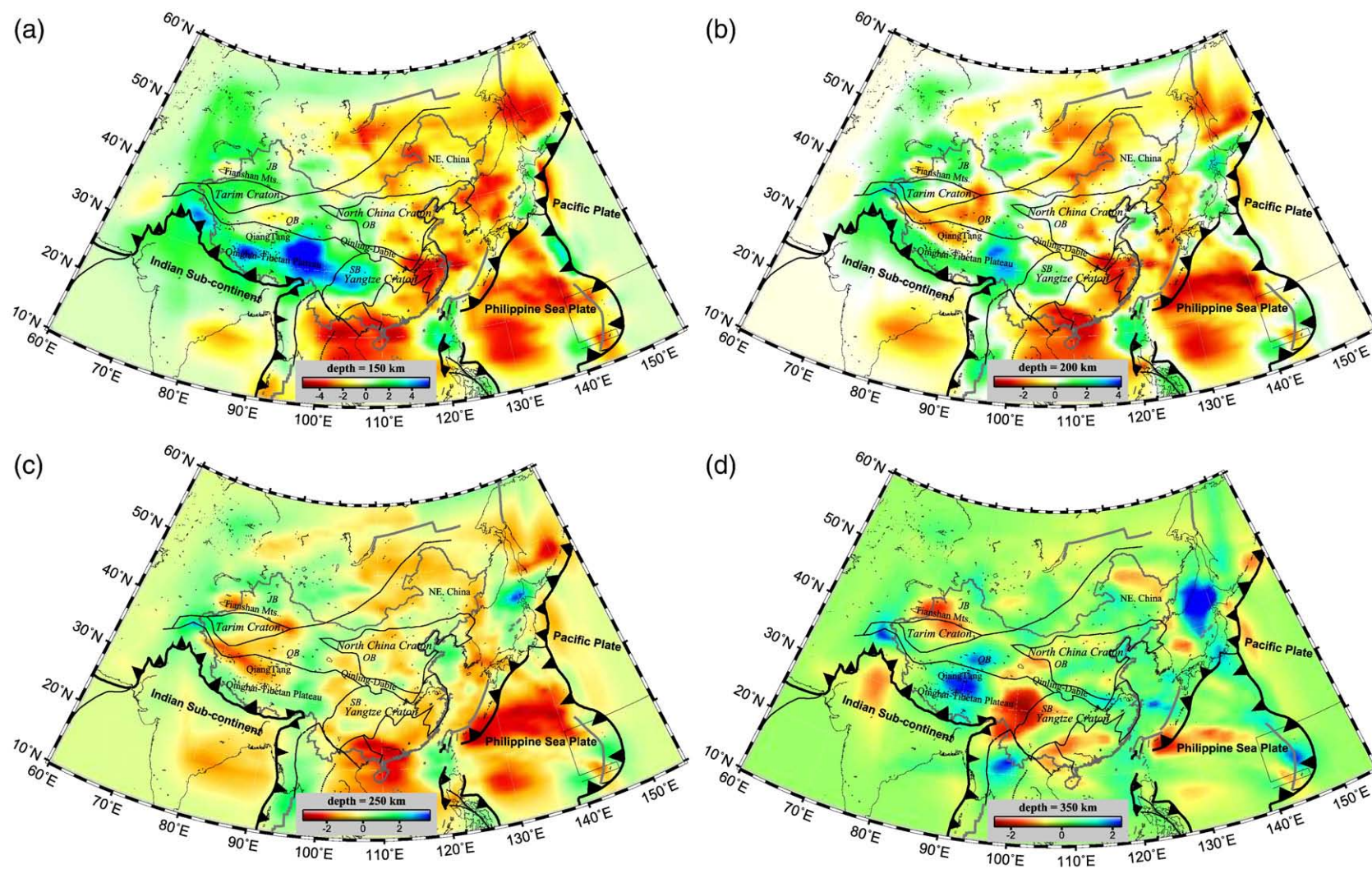


Fig. 5. S-wave velocities at depths of 150 km (a), 200 km (b), 250 km (c), and 350 km (d).

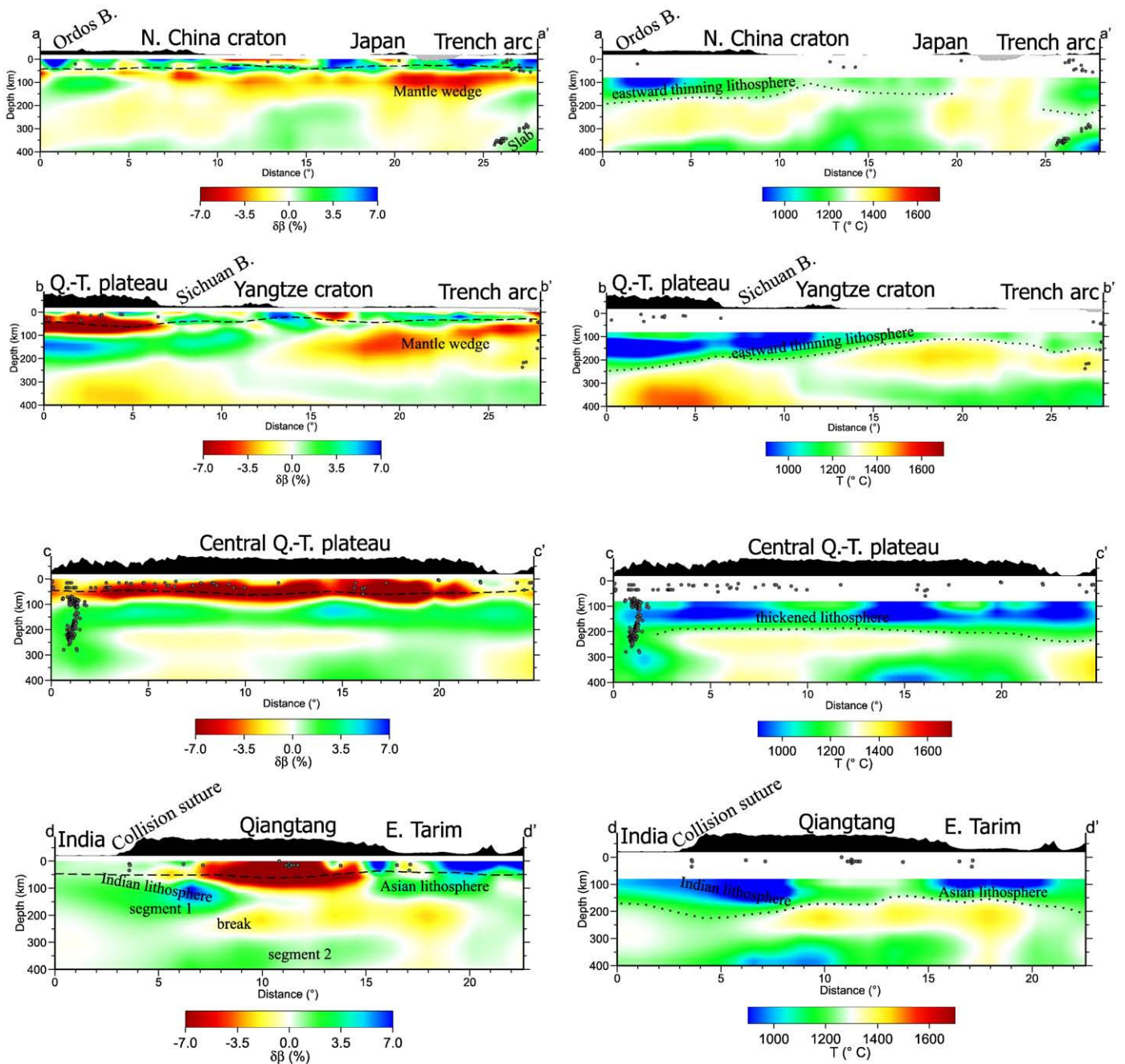


Fig. 6. S-wave velocities (left) and temperatures (right) in various vertical transects. Transect locations are shown in Fig. 1. Dashed lines on the S-wave velocity transects indicate Moho depth, and dotted lines on the temperature transects indicate the estimated base of the lithosphere. Above each transect, exaggerated topography is shown in black for positive elevation and gray for negative elevation. Hypocenters of past earthquakes in the EHB catalogue (Engdahl et al., 1998) are shown as gray points.

mainly traverses the North China craton and shows a marked variation in lithosphere thickness from west (>150 km) to east (~ 100 km) (see the dotted line on temperature transect a–a'). Except for the high lithospheric velocities beneath the Ordos Basin in the west, most of the North China craton is underlain by low velocities at depths of ~ 50 – 300 km. The low-velocity layer in transect a–a' shows a trend of increasing velocity from the subduction zone to the central craton. The western part of transect b–b' crosses part of the eastern Qinghai-Tibetan Plateau, entirely within the Yangtze craton. Again, the lithospheric thickness of the Yangtze craton shows a pronounced thinning from west (~ 200 km) to east (~ 100 km), and on the east side of the transect the cratonic lithosphere is underlain by a low-velocity layer. Below 300 km depth in transects a–a' and b–b', velocities are fastest and temperatures coolest where the cratonic lithosphere is thinnest.

Transects c–c' and d–d' (Fig. 6) mainly cross the Qinghai-Tibetan Plateau and surrounding areas in western China. A common feature imaged in these transects is thick lithosphere (~ 200 km) beneath almost the entire Qinghai-Tibetan Plateau, except around Qiangtang in the northern part of the plateau. The transect c–c' is oriented parallel to the syntaxis of Indo-Asian collision, and mainly covers the southern Qinghai-Tibetan Plateau. The westernmost part of transect c–c' is located near the margin of the present study region, and is therefore relatively poorly resolved. Nevertheless, this area contains very thick lithosphere (>350 km), consistent with the occurrence of deep earthquakes associated with cold and therefore relatively rigid parts of the mantle, most likely with subducted lithosphere resulting from convergence between India and Asia. The remaining part of transect c–c' shows a relatively homogenous high-velocity lithosphere

down to 200 km, beneath which low velocities are imaged at 200–400 km depth beneath the central plateau.

Transect d–d' is oriented perpendicular to the syntaxis of Indo-Asian collision. Both Indian and Asian lithosphere are well imaged as high-velocity zones, separated by a mushroom-shaped low-velocity anomaly, with its cap located beneath Qiangtang and its stem beneath the area east of Tarim. The Indian lithosphere appears to be broken into two segments with different horizontal and vertical extents (labeled “segment 1” and “segment 2” in Fig. 6). The segment beneath India and the southern part of the plateau (segment 1) extends no deeper than 300 km, whereas the segment beneath Qiangtang (segment 2) lies at depths greater than 300 km. These segments are discussed in detail below.

6. Discussion

6.1. Eastern China

As described above, the North China craton and the Yangtze craton are characterized by lithosphere that thins from west to east. For the Yangtze craton this thinning is accompanied by a low-velocity layer that becomes more pronounced from west to east. The thinning of the North China craton has been extensively studied (e.g., Chen et al., 1991; Menzies et al., 1993; Yuan, 1996; Fan et al., 2000; Chen et al., 2001; O'Reilly et al., 2001; Xu, 2001; Zheng et al., 2001; An and Shi, 2006; Menzies et al., 2007; Xu et al., 2008), and it has been proposed that the low velocities in the east result from hot partial melts or fluids ascending from the westward-subducting sub-horizontal oceanic slab in the mantle transition zone. Such partial melts can erode the base of the overlying lithosphere, ultimately resulting in lithosphere thinning via removal of the eroded lithosphere root. Alternatively, such melts could metasomatize or refertilize the craton *in situ*, particularly if accompanied by volatiles (Menzies et al., 1993; Lee et al., 1996; Griffin et al., 1998; Pearson, 1999; Zheng et al., 2007).

These possibilities appear reasonable in the present case because there exists ample evidence for the existence of a sub-horizontal oceanic slab in the mantle transition zone (e.g., van der Hilst et al., 1991, 1997; Fukao et al., 1992, 2001; Pysklywec and Ishii, 2005; Huang and Zhao, 2006). Magmatism at the eastern edge of the North China craton at 135–127 Ma has been linked with the upwelling of asthenosphere caused by subduction of the Paleo-Pacific plate (Wilde et al., 2003; Chen et al., 2005, 2007).

The present seismic model shows slightly high velocities at 200–400 km depth beneath the Yangtze craton (Fig. 6, profile b–b') and high velocities at 250–400 km depth beneath the eastern North China craton. It is unclear whether the middle upper-mantle contains a delaminated but rigid piece of lithosphere or whether the average velocity in this zone beneath eastern China is slightly higher than the global average. The lateral continuity of the high-velocity layer beneath the low-velocity layer suggests that upwelling may ascend through localized vertical channels rather than uniformly from the entire subducted slab in the transition zone (e.g., An et al., 2009). The localized upward flow can ultimately induce lateral flow of hot buoyant material along the base of the lithosphere (Davies, 1988; Sleep, 1990).

6.2. Western China

Western China is bound to the southwest by the Indian subcontinent, where Indo-Asian collision started at ~50 Ma (e.g., Searle et al., 1987; Royden et al., 2008), immediately after completion of the subduction of the Tethyan oceanic plate beneath Eurasia. The influence of Indo-Asian collision on western China has left a clear footprint on the seismic–thermal structures of the upper mantle.

In western China, a weak northward-dipping high-velocity anomaly, which probably represents the Indian lithosphere, is imaged beneath

the southern Qinghai-Tibetan Plateau with a roughly east–west extension, parallel to the syntaxis of Indo-Asian collision (transects c–c' and d–d' in Fig. 6). However, the high-velocity Indian lithosphere does not appear to continue further north beneath Qiangtang, which is underlain by low velocities down to ~300 km depth (transect d–d'). Deep-level low velocities are also imaged beneath the area east of Tarim, representing a northward extension of the relatively shallow low velocities imaged beneath Qiangtang (transect d–d'). This low-velocity pattern resembles a mushroom, with its cap located beneath Qiangtang and its stem beneath the area east of Tarim.

The area beneath Qiangtang is characterized by the absence of high-velocity lithosphere and a widespread, strong low-velocity anomaly, the origin of which remains under debate. This low-velocity anomaly beneath Qiangtang was imaged previously by a regional teleseismic–tomographic study (Tilmann et al., 2003) and surface-wave tomographic studies (Friederich, 2003; Huang et al., 2003; Priestley et al., 2006). Tilmann et al. (2003) imaged low velocities beneath Qiangtang that extend downward to at least 400 km depth. South of this low-velocity anomaly, beneath central Tibet, the authors imaged high velocities and suggested that the low velocities beneath Qiangtang might represent a convection cell located north of the area of northward subduction of Indian lithosphere. A study of shear wave splitting (Huang et al., 2000) imaged significant anisotropy beneath the Qiangtang block but negligible anisotropy in central Tibet to the south, supporting the model in which low velocities beneath Qiangtang reflect mantle material squeezed out by convergence between the Indian and Asian lithospheres. Because of insufficient path coverage, Friederich (2003) imaged normal to slightly low velocities down to 250 km depth beneath Qiangtang, rather than a strong low-velocity anomaly; however, he did image a weak high-velocity anomaly with a gentle southward dip beneath the northern margin of the plateau, which could represent Asian lithosphere and thereby support the “squeeze-out” model.

The present model, with better path coverage in western China, imaged low velocities beneath Qiangtang that are connected with the deep-level low velocities beneath the area east of Tarim (i.e., the mushroom-shaped low-velocity anomaly). We suggest that the deeper and weaker low velocities beneath the area east of Tarim may have existed prior to Indo-Asian collision and are possibly related to subduction of Tethyan Ocean lithosphere beneath the Eurasian continent. The low-velocity material was subsequently pushed to its present position by the northeastward-subducting sub-horizontal Indian lithospheric slab.

As stated above, transect d–d' shows two high-velocity segments beneath the Qinghai-Tibetan Plateau: one beneath India and the southern plateau at depths less than 300 km, and the other beneath Qiangtang at depths greater than 300 km. It is logical to interpret the shallow high-velocity segment (segment 1) as the young, subducting Indian lithosphere. The north–south extent of the deep-level high-velocity segment (segment 2) is ~1400 km (~13° of great circle distance), located far from the suture zone of Indo-Asian collision. Paleomagnetic data indicate that 1000–1500 km of Indian continental lithosphere has been consumed in the Himalayas (Chen et al., 1993; Patzelt et al., 1996), similar to the extent of the deep high-velocity anomaly (segment 2). Accordingly, segment 2 is interpreted to be related to the older subducted Indian lithosphere. If both the shallow and deep high-velocity segments are related to subducted Indian lithosphere, the deep older Indian slab must have broken off from the shallower portion after the initial Indo-Asian collision at ~50 Ma.

The northward extent of the shallow segment of Indian lithosphere is ~400 km from the suture zone of the collision (i.e., the point labeled “break” on transect d–d'). Based on a convergence rate between the Indian and Asian plates of ~20 km/m.y. (Bilham et al., 1997), a movement of 400 km requires ~20 m.y., indicating that the Indian lithospheric slab might have broken off as early as ~20 Ma. This result not only confirms the timing of break-off of the deeper portion

of the subducting slab from the shallower portion suggested by Chemenda et al. (2000), but also coincides with the time (~15 to 20 Ma) when fragment extrusion beyond the plateau slowed down and contributed to the onset of rapid surface uplift and crustal thickening in eastern Tibet (Royden et al., 2008). Thus, the modern structural system that currently accommodates deformation within Tibet may have started at around 20 Ma (Royden et al., 2008).

What caused the deeper portion of the subducting Indian slab to break off from the shallower portion at ~20 Ma? The crust of the Qinghai-Tibetan Plateau is thicker than that of the Indian continent (Laske et al., 2000; Shin et al., 2007), possibly making the Qinghai-Tibetan Plateau slightly more buoyant than the Indian lithosphere. Accordingly, it is possible that the negative buoyancy of the Indian lithosphere causes it to subduct beneath (underthrust) the Qinghai-Tibetan Plateau. Alternatively, or in addition, slab pull from the still-attached part of the subducted Indian lithosphere could have been strong enough to force continental India beneath the Qinghai-Tibetan Plateau. The Indian lithosphere is continental type, with a similar composition to the Qinghai-Tibetan lithosphere. Upon subduction, the continental slab would have been heated, meaning that the negative buoyancy of the slab would have changed to neutral or positive buoyancy, thereby overcoming the slab pull force. Given the scenario of the shallow portion of the subducting slab resisting continued subduction and the deep portion pulling further down, the subducted lithosphere would have broken to form two slab segments beneath the plateau, as imaged as segments 1 and 2 in the present study.

Previous studies have shown that a pure oceanic-type slab (e.g., Tethyan oceanic slab) is very dense and can detach from the continental part of the lithosphere and sink into the transition zone (400–600 km deep) or lower mantle (>660 km) (Van der Voo et al., 1999; Chemenda et al., 2000); however, the present model shows that segment 2 of the subducting Indian slab lies immediately beneath segment 1, and has not sunk down to the transition zone as expected for an oceanic-type slab. One possible explanation for this observation is that segment 2 is intermediate in nature/composition between continental and oceanic lithosphere (e.g., foreland), resulting in stronger negative buoyancy than the light segment 1 (old, stable continental lithosphere) and weaker negative buoyancy than the dense, subducting oceanic slab. According to this interpretation, break-off of the subducting Indian lithosphere into two segments, as indicated in the present model, may have been caused by contrasts in lithosphere, and thus in composition. Moreover, a change in the composition of the subducting Indian slab may affect the geodynamic behavior of the overlying lithosphere. The modern structural system of the Qinghai-Tibetan Plateau may have initiated at ~20 Ma, at the same time as the onset of subduction of the old, stable Indian continental lithosphere (segment 1).

7. Conclusions

The joint inversion of regional multimode surface waveforms and fundamental-mode surface-wave dispersion curves combines the advantage of the good path coverage of fundamental-mode dispersion measurements and the good sensitivity to deep structures of the multimode waveforms. This approach enabled us to produce a well-constrained 3-D upper-mantle S-wave velocity model for China. The agreement between the detailed structures imaged using the sophisticated 3-D upper-mantle model constrained by exact 3-D waveform sensitivity kernels confirms that the use of physically-based regularization and a large amount of surface-wave data can counterbalance the shortcomings of ray theory in considering finite-frequency effects. The conversion of upper-mantle tomographic S-wave velocity to temperature is a viable method of estimating lithosphere thickness.

The final seismic-thermal model produced in the present study highlights interesting structural features in the upper mantle beneath China. In eastern China, the North China craton and the Yangtze craton are characterized by marked spatial variations in lithospheric

thickness, with the lithosphere thinning from west to east. The underlying low-velocity layer and deeper high velocities provide important clues regarding the cause of this thinning. The low velocities are interpreted to reflect hot partial melts or fluids ascending from the westward-subducting, sub-horizontal oceanic slab in the mantle transition zone; such partial melts can erode or refertilize the overlying lithosphere base and eventually result in lithosphere thinning. Beneath western China, thickened lithosphere is imaged beneath the Qinghai-Tibetan Plateau, except for beneath Qiangtang on the northern plateau, which is underlain by low velocities. The present model generally supports the hypothesis that low velocities beneath Qiangtang reflect material squeezed out by convergence between the Indian and Asian lithospheres. The identification of two segments of subducted lithosphere suggests that the Indian lithosphere might have fractured and broken as long ago as 20 Ma.

Acknowledgements

We thank the China Earthquake Data Center and DMC of IRIS for providing seismic data. This work was supported by the National Natural Science Foundation of China (grants 40504011 and 40674058) and the Fundamental Scientific Research Fund of the Institute of Geomechanics, Chinese Academy of Geological Sciences (DZLXJK200707). All figures were prepared using the Generic Mapping Tools (Wessel and Smith, 1991).

References

- An, M., Assumpção, M.S., 2006. Crustal and upper mantle structure in intracratonic Paraná Basin, SE Brazil, from surface wave dispersion using genetic algorithm. *Journal of South American Earth Sciences* 21 (3), 173–184.
- An, M., Shi, Y., 2006. Lithospheric thickness of the Chinese continent. *Physics of the Earth and Planetary Interiors* 159, 257–266.
- An, M., Shi, Y., 2007. 3D crustal and upper-mantle temperature of the Chinese continent. *Science in China Series D: Earth Sciences* 50 (10), 1441–1451.
- An, M., Feng, M., Zhao, Y., 2009. Destruction of lithosphere within the North China Craton inferred from surface wave tomography. *Geochemistry Geophysics Geosystems* 10 (8), Q08016.
- Artemieva, I.M., Mooney, W.D., 2001. Thermal thickness and evolution of Precambrian lithosphere: a global study. *Journal of Geophysical Research* 106 (B8), 16387–16414.
- Avseth, P., Mukerji, T., Mavko, G., 2005. *Quantitative Seismic Interpretation: Applying Rock Physics Tools to Reduce Interpretation Risk*. Cambridge University Press, 359 pp.
- Bilham, R., Larson, K., Freymueller, J., 1997. GPS measurements of present-day convergence across the Nepal Himalaya. *Nature* 386 (6620), 61–64.
- Cammarano, F., Goes, S., Vacher, P., Giardini, D., 2003. Inferring upper-mantle temperatures from seismic velocities. *Physics of the Earth and Planetary Interiors* 138 (3–4), 197–222.
- Chemenda, A.I., Burg, J.-P., Mattauer, M., 2000. Evolutionary model of the Himalaya-Tibet system: geopoem: based on new modelling, geological and geophysical data. *Earth and Planetary Science Letters* 174 (3–4), 397–409.
- Chen, G.-Y., Song, Z.-H., An, C.-Q., Cheng, L.-H., Zhuang, Z., Fu, Z.-W., Lu, Z.-L., Hu, J.-F., 1991. Three-dimensional crust and upper mantle structure of the North China region. *Acta Geophysica Sinica* 34 (2), 172–181.
- Chen, Y., Courtillot, V., Cogné, J.-P., Besse, J., Yang, Z., Enkin, R., 1993. The configuration of Asia prior to the collision of India: Cretaceous paleomagnetic constraints. *Journal of Geophysical Research* 98 (B12), 21927–21941.
- Chen, S., O'Reilly, S.Y., Zhou, X., Griffin, W.L., Zhang, G., Sun, M., Feng, J., Zhang, M., 2001. Thermal and petrological structure of the lithosphere beneath Hannuoba, Sino-Korean Craton, China: evidence from xenoliths. *Lithos* 56 (4), 267–301.
- Chen, B., Tian, W., Zhai, M., Arakawa, Y., 2005. Zircon U–Pb geochronology and geochemistry of the Mesozoic magmatism in the Taihang Mountains and other places of the North China craton, with implications for petrogenesis and geodynamic setting. *Acta Petrologica Sinica* 21 (1), 13–24.
- Chen, B., Zhai, M.-G., Tian, W., 2007. Origin of the Mesozoic magmatism in the North China Craton: constraints from petrological and geochemical data. *Geological Society, London, Special Publications* 280 (1), 131–151.
- Chen, L., Tao, W., Zhao, L., Zheng, T., 2008. Distinct lateral variation of lithospheric thickness in the Northeastern North China Craton. *Earth and Planetary Science Letters* 267, 56–68.
- Darby, B.J., Ritts, B.D., Yue, Y., Meng, Q., 2005. Did the Altyn Tagh fault extend beyond the Tibetan Plateau? *Earth and Planetary Science Letters* 240, 425–435.
- Davies, G.F., 1988. Ocean bathymetry and mantle convection 1. Large-scale flow and hotspots. *Journal of Geophysical Research* 93 (B9), 10467–10480.
- Dziewonski, A.M., Friedman, A., Giardini, D., Woodhouse, J.H., 1983. Global seismicity of 1982: centroid-moment tensor solutions for 308 earthquakes. *Physics of the Earth and Planetary Interiors* 33, 76–90.

- Engdahl, E.R., van der Hilst, R.D., Buland, R., 1998. Global teleseismic earthquake relocation with improved travel times and procedures for depth determination. *Bulletin of the Seismological Society of America* 88, 722–743.
- Fan, W.M., Zhang, H.F., Baker, J., Jarvis, K.E., Mason, P.R.D., Menzies, M.A., 2000. On and off the North China Craton: where is the Archaean keel? *Journal of Petrology* 41 (7), 933–950.
- Feng, M., Assumpção, M.S., van der Lee, S., 2004. Group-velocity tomography and lithospheric S-velocity structure of the South American continent. *Physics of the Earth and Planetary Interiors* 147, 315–331.
- Feng, M., Van der Lee, S., Assumpção, M., 2007. Upper mantle structure of South America from joint inversion of waveforms and fundamental-mode group velocities of Rayleigh waves. *Journal of Geophysical Research* 112, B04312.
- Friederich, W., 2003. The S-velocity structure of the East Asian mantle from inversion of shear and surface waveforms. *Geophysical Journal International* 153, 88–102.
- Fukao, Y., Obayashi, M., Inoue, H., Nishii, M., 1992. Subducting slabs stagnant in the mantle transition zone. *J. Geophys. Res.* 97 (B4), 4809–4822.
- Fukao, Y., Widiyantoro, S., Obayashi, M., 2001. Stagnant slabs in the upper and lower mantle transition region. *Rev. Geophys.* 39 (3), 291–323.
- Galvé, A., Sabin, M., Hirn, A., Diaz, J., Lépine, J.C., Laigle, M., Gallart, J., Jiang, M., 2002. Complex images of Moho and variation of V_p/V_s across the Himalaya and South Tibet, from a joint receiver-function and wide-angle-reflection approach. *Geophysical Research Letters* 29 (24), 2182.
- Gao, X., Wang, W.M., Yao, Z.X., 2005. Crustal structure of China mainland and its adjacent regions. *Chinese Journal of Geophysics (in Chinese)* 48 (3), 591–601.
- Goes, S., Van der Lee, S., 2002. Thermal structure of the North American uppermost mantle inferred from seismic tomography. *Journal of Geophysical Research* 107 (B3), 2050.
- Goes, S., Govers, R., Vacher, P., 2000. Shallow mantle temperatures under Europe from P and S wave tomography. *Journal of Geophysical Research* 105 (B5), 11153–11169.
- Griffin, W.L., Zhang, A., O'Reilly, S.Y., Ryan, C.G., 1998. Phanerozoic evolution of the lithosphere beneath the Sino-Korean craton. In: Flower, M.F.J., Chung, S.-L., Lo, C.-H., Lee, T.-Y. (Eds.), *Mantle Dynamics and Plate Interactions in East Asia*. American Geophysical Union, Washington, D.C., pp. 107–126.
- Griffin, W.L., Ryan, C.G., Kaminsky, F.V., O'Reilly, S.Y., Natapov, L.M., Win, T.T., Kinny, P.D., Ilupin, I.P., 1999. The Siberian lithosphere traverse: mantle terranes and the assembly of the Siberian Craton. *Tectonophysics* 310 (1–4), 1–35.
- Hirth, G., Kohlstedt, D.L., 1996. Water in the oceanic upper mantle: implications for rheology, melt extraction and the evolution of the lithosphere. *Earth and Planetary Science Letters* 144, 93–108.
- Huang, J., Zhao, D., 2006. High-resolution mantle tomography of China and surrounding regions. *Journal of Geophysical Research* 111 (B9), B09305.
- Huang, W.C., Ni, J.F., Tilmann, F., Nelson, D., Guo, J., Zhao, W., Mechie, J., Kind, R., Saul, J., Rapine, R., Hearn, T.M., 2000. Seismic polarization anisotropy beneath the central Tibetan Plateau. *Journal of Geophysical Research* 105 (B12), 27979–27989.
- Huang, Z., Su, W., Peng, Y., Zheng, Y., Li, H., 2003. Rayleigh wave tomography of China and adjacent regions. *Journal of Geophysical Research* 108 (B2), 2073.
- Jordan, T.H., 1979. Mineralogies, densities and seismic velocities of garnet lherzolites and their geophysical implications. In: Boyd, F.R., Myer, H.O.A. (Eds.), *The Mantle Sample: Inclusions in Kimberlites and Other Volcanics*. AGU, Washington, D.C., pp. 1–14.
- Karato, S.-I., Jung, H., 1998. Water, partial melting and the origin of the seismic low velocity and high attenuation zone in the upper mantle. *Earth and Planetary Science Letters* 157, 193–207.
- Kennett, B.L.N., Engdahl, E.R., 1991. Traveltimes for global earthquake location and phase identification. *Geophysical Journal International* 105, 429–465.
- Laske, G., Masters, G., Reif, C., 2000. CRUST2.0: a New Global Crustal Model at $2^\circ \times 2^\circ$.
- Lebedev, S., Nolet, G., 2003. Upper mantle beneath Southeast Asia from S velocity tomography. *Journal of Geophysical Research* 108 (B1), 2048.
- Lee, D.-C., Halliday, A.N., Davies, G.R., Essene, E.J., Fitton, J.G., Temdjim, R., 1996. Melt enrichment of shallow depleted mantle: a detailed petrological, trace element and isotopic study of mantle-derived xenoliths and megacrysts from the Cameroon line. *Journal of Petrology* 37 (2), 415–441.
- Li, C., van der Hilst, R.D., Toksoz, M.N., 2006a. Constraining P-wave velocity variations in the upper mantle beneath Southeast Asia. *Physics of the Earth and Planetary Interiors* 154, 180–195.
- Li, S.L., Mooney, W.D., Fan, J.C., 2006b. Crustal structure of mainland China from deep seismic sounding data. *Tectonophysics* 420, 239–252.
- Mangino, S., Priestley, K., Ebel, J., 1999. The receiver structure beneath the China Digital Seismograph Network stations. *Bulletin of the Seismological Society of America* 89 (4), 1053–1076.
- McDonough, W.F., Rudnick, R.L., 1998. Mineralogy and composition of the upper mantle. In: Hemley, R.J. (Ed.), *Ultrahigh-pressure Mineralogy: Physics and Chemistry of the Earth's Deep Interior*. Mineralogical Society of America, Washington, DC, pp. 139–164.
- McKenzie, D., Priestley, K., 2008. The influence of lithosphere thickness variations on continental evolution. *Lithos* 102, 1–11.
- Menzies, M.A., Xu, Y.-G., 1998. Geodynamics of the North China Craton. In: Flower, M.F.J., Chung, S.-L., Lo, C.-H., Lee, T.-Y. (Eds.), *Mantle Dynamics and Plate Interactions in East Asia*. American Geophysical Union, Washington, D.C., pp. 155–165.
- Menzies, M.A., Fan, W., Zhang, M., 1993. Palaeozoic and Cenozoic lithoprobes and the loss of >120 km of Archaean lithosphere, Sino-Korean craton, China. *Magmatic Processes and Plate Tectonics*, 76. Geological Society, London, Special Publications, 71–81 pp.
- Menzies, M., Xu, Y., Zhang, H., Fan, W., 2007. Integration of geology, geophysics and geochemistry: a key to understanding the North China Craton. *Lithos* 96, 1–21.
- Nolet, G., Zielhuis, A., 1994. Low S velocities under the Tornquist-Teisseyre zone: evidence for water injection into the transition zone by subduction. *Journal of Geophysical Research* 99, 15813–15820.
- O'Reilly, S.Y., Griffin, W.L., 2006. Imaging global chemical and thermal heterogeneity in the subcontinental lithospheric mantle with garnets and xenoliths: geophysical implications. *Tectonophysics* 416, 289–309.
- O'Reilly, S.Y., Griffin, W.L., Djoman, Y.H.P., Morgan, P., 2001. Are lithospheres forever? Tracking changes in subcontinental lithospheric mantle through time. *GSA Today* 11 (4), 4–10.
- Paige, C.C., Saunders, M.A., 1982a. Algorithm 583, LSQR: sparse linear equations and least squares problems. *ACM Transactions on Mathematical Software* 8 (2), 195–209.
- Paige, C.C., Saunders, M.A., 1982b. LSQR: an algorithm for sparse linear equations and sparse least squares. *ACM Transactions on Mathematical Software* 8 (2), 43–71.
- Patzelt, A., Li, H., Wang, J., Appel, E., 1996. Palaeomagnetism of Cretaceous to Tertiary sediments from southern Tibet: evidence for the extent of the northern margin of India prior to the collision with Eurasia. *Tectonophysics* 259 (4), 259–284.
- Pearson, D.G., 1999. The age of continental roots. *Lithos* 48 (1–4), 171–194.
- Priestley, K., Debayle, E., 2003. Seismic evidence for a moderately thick lithosphere beneath the Siberian Platform. *Geophysical Research Letters* 30 (3), 1118.
- Priestley, K., McKenzie, D., 2006. The thermal structure of the lithosphere from shear wave velocities. *Earth and Planetary Science Letters* 244, 285–301.
- Priestley, K., Debayle, E., McKenzie, D., Piliidou, S., 2006. Upper mantle structure of eastern Asia from multimode surface waveform tomography. *Journal of Geophysical Research* 111, B10304.
- Pysklywec, R.N., Ishii, M., 2005. Time dependent subduction dynamics driven by the instability of stagnant slabs in the transition zone. *Phys. Earth Planet. In.* 149, 115–132.
- Rapine, R., Tilmann, F., West, M., Ni, J., Rodgers, A., 2003. Crustal structure of northern and southern Tibet from surface wave dispersion analysis. *Journal of Geophysical Research* 108 (B2), 2120.
- Ren, J., Wang, Z., Chen, B., Jiang, C., Niu, B., Li, J., Xie, G., He, Z., Liu, Z., 1999. The Tectonics of China from a Global View – a Guide to the Tectonic Map of China and Adjacent Regions. Geological Publishing House, Beijing, 32 pp.
- Replumaz, A., Káráson, H., van der Hilst, R.D., Besse, J., Tapponnier, P., 2004. 4-D evolution of SE Asia's mantle from geological reconstructions and seismic tomography. *Earth and Planetary Science Letters* 221, 103–115.
- Ritzwoller, M.H., Levshin, A.L., 1998. Eurasian surface wave tomography: group velocities. *Journal of Geophysical Research* 103 (B3), 4839–4878.
- Ritzwoller, M.H., Shapiro, N.M., Barmin, M.P., Levshin, A.L., 2002. Global surface wave diffraction tomography. *Journal of Geophysical Research* 107 (B12), 2335.
- Royden, L.H., Burchfiel, B.C., van der Hilst, R.D., 2008. The geological evolution of the Tibetan Plateau. *Science* 321 (5892), 1054–1058.
- Schuberth, B.S.A., Bunge, H.P., Ritsma, J., 2009. Tomographic filtering of high-resolution mantle circulation models: can seismic heterogeneity be explained by temperature alone? *Geochemistry Geophysics Geosystems* 10 (5), Q05W03.
- Searle, M.P., Windley, B.F., Coward, M.P., Cooper, D.J.W., Rex, A.J., Rex, D., Tingdong, L., Xuchang, X., Jan, M.Q., Thakur, V.C., Kumar, S., 1987. The closing of Tethys and the tectonics of the Himalaya. *Geological Society of America Bulletin* 98 (6), 678–701.
- Shapiro, N.M., Ritzwoller, M.H., 2002. Monte-Carlo inversion for a global shear-velocity model of the crust and upper mantle. *Geophysical Journal International* 151, 88–105.
- Shapiro, N.M., Ritzwoller, M.H., 2004. Thermodynamic constraints on seismic inversions. *Geophysical Journal International* 157, 1175–1188.
- Shin, Y.H., Xu, H., Braitenberg, C., Fang, J., Wang, Y., 2007. Moho undulations beneath Tibet from GRACE-integrated gravity data. *Geophysical Journal International* 170 (3), 971–985.
- Sieminski, A., Lévêque, J.-J., Debayle, E., 2004. Can finite-frequency effects be accounted for in ray theory surface wave tomography? *Geophysical Research Letters* 31, L24614.
- Simons, F.J., van der Hilst, R.D., 2002. Age-dependent seismic thickness and mechanical strength of the Australian lithosphere. *Geophysical Research Letters* 29 (11), 1529.
- Sleep, N.H., 1990. Hotspots and mantle plumes: some phenomenology. *Journal of Geophysical Research* 95 (B5), 6715–6736.
- Snoke, J.A., James, D.E., 1997. Lithospheric structure of the Chaco and Paraná Basins of South America from surface-wave inversion. *Journal of Geophysical Research* 102, 2939–2951.
- Snoke, J.A., Sambridge, M., 2002. Constraints on the S wave velocity structure in a continental shield from surface wave data: comparing linearized least squares inversion and the direct search Neighbourhood Algorithm. *Journal of Geophysical Research* 107 (B5), 2094.
- Sobolev, S.V., Zeyen, H., Stoll, G., Werling, F., Altherr, R., Fuchs, K., 1996. Upper mantle temperatures from teleseismic tomography of French Massif Central including effects of composition, mineral reactions, anharmonicity, anelasticity and partial melt. *Earth and Planetary Science Letters* 139 (1–2), 147–163.
- Tilmann, F., Ni, J., INDEPTH III Seismic Team, 2003. Seismic imaging of the downwelling Indian lithosphere beneath central Tibet. *Science* 300, 1424–1427.
- van der Hilst, R.D., Engdahl, E.R., Spakman, W., Nolet, G., 1991. Tomographic imaging of subducted lithosphere below northwestern Pacific island arcs. *Nature* 353, 37–42.
- van der Hilst, R.D., Widiyantoro, S., Engdahl, E.R., 1997. Evidence for deep mantle circulation from global tomography. *Nature* 386, 578–584.
- Van der Lee, S., 2001. Deep below North America. *Science* 294 (5545), 1297–1298.
- Van der Lee, S., 2002. High-resolution estimates of lithosphere thickness from Missouri to Massachusetts, USA. *Earth and Planetary Science Letters* 203, 15–23.
- Van der Lee, S., Nolet, G., 1997. Upper-mantle S velocity structure of North America. *Journal of Geophysical Research* 102, 22815–22838.
- Van der Lee, S., James, D., Silver, P., 2001. Upper mantle S velocity structure of central and western South America. *Journal of Geophysical Research* 106 (B12), 30821–30834.
- Van der Voo, R., Spakman, W., Bijwaard, H., 1999. Tethyan subducted slabs under India. *Earth and Planetary Science Letters* 171, 7–20.

- Wessel, P., Smith, W.H.F., 1991. Free software helps map and display data. *EOS Transactions, American Geophysical Union* 72, 441.
- Wilde, S.A., Zhou, X., Nemchin, A.A., Sun, M., 2003. Mesozoic crust–mantle interaction beneath the North China craton: a consequence of the dispersal of Gondwanaland and accretion of Asia. *Geology* 31 (9), 817–820.
- Xu, X., Griffin, W.L., O'Reilly, S.Y., Pearson, N.J., Geng, H., Zheng, J., 2008. Re–Os isotopes of sulfides in mantle xenoliths from eastern China: progressive modification of lithospheric mantle. *Lithos* 102 (1–2), 43–64.
- Xu, Y.-G., 2001. Thermo-tectonic destruction of the Archaean lithospheric keel beneath the Sino-Korean Craton in China: evidence, timing and mechanism. *Physics and Chemistry of the Earth (A)* 26 (9–10), 747–757.
- Yuan, X., 1996. Velocity structure of the Qinling lithosphere and mushroom cloud model. *Science in China Series D: Earth Sciences* 39 (3), 235–244.
- Zheng, J., O'Reilly, S.Y., Griffin, W.L., Lu, F., Zhang, M., Pearson, N.J., 2001. Relict refractory mantle beneath the eastern North China block: significance for lithosphere evolution. *Lithos* 57, 43–66.
- Zheng, J.P., Griffin, W.L., O'Reilly, S.Y., Yu, C.M., Zhang, H.F., Pearson, N., Zhang, M., 2007. Mechanism and timing of lithospheric modification and replacement beneath the eastern North China Craton: peridotitic xenoliths from the 100 Ma Fuxin basalts and a regional synthesis. *Geochimica et Cosmochimica Acta* 71 (21), 5203–5225.